

Imaging the local electronic and magnetic properties of intrinsically phase separated $\text{Rb}_x\text{Fe}_{2-y}\text{Se}_2$ superconductor using scanning microscopy techniques

P Dudin¹ , D Herriott², T Davies², A Krzton-Maziopa³ , E Pomjakushina⁴, K Conder⁴, C Cacho¹, J R Yates² and S C Speller² 

¹ Diamond Light Source, University of Oxford, Oxford, OX1 3PU, United Kingdom

² Department of Materials, University of Oxford, Oxford, OX1 3PH, United Kingdom

³ Warsaw University of Technology, Faculty of Chemistry, Noakowskiego St. 3, 00-664 Warsaw, Poland

⁴ Laboratory for Multiscale Materials Experiments (LMX), Paul Scherrer Institute, CH-5232 Villigen PSI, Switzerland

E-mail: susannah.speller@materials.ox.ac.uk

Received 4 December 2018, revised 8 January 2019

Accepted for publication 17 January 2019

Published 27 February 2019



CrossMark

Abstract

The discovery in 2008 of the iron-based superconducting pnictide and chalcogenide compounds has provided an entirely new family of materials for studying the crucial interplay between superconductivity and magnetism in unconventional superconductors. The alkali-metal-intercalated iron selenide ($\text{A}_x\text{Fe}_{2-y}\text{Se}_2$, A = alkali metal) superconductors are of particular interest owing to their relatively high transition temperatures over 30 K and the co-existence of the superconducting state with antiferromagnetic ordering. Intrinsic phase separation on the mesoscopic scale is known to occur in ‘single crystals’ of these compounds, adding to the complexity of interpretation of bulk property measurements. In this study, we investigate the local electronic structure and chemistry of $\text{Rb}_x\text{Fe}_{2-y}\text{Se}_2$ crystals using scanning microscopy techniques. Nano-focussed angle-resolved photoemission spectroscopy has enabled the band structure of the minority superconducting phase and the non-superconducting matrix to be measured independently and linked to the surface chemistry from the same regions using core level spectroscopy. Valence band mapping reveals the characteristic microstructure of these crystals, but does not have sufficient spatial resolution to enable the precise morphology of the superconducting phase to be elucidated. Cryogenic magnetic force microscopy has shown that the superconducting phase has a fine-scale stripey morphology that was not resolved in the scanning photoemission spectroscopy experiment. The correlation of these findings with previous microstructural studies, bulk measurements and first-principles density functional theory calculations paves the way for understanding the intriguing electronic and magnetic properties of these compounds.

Supplementary material for this article is available [online](#)

Keywords: iron-based superconductor, ARPES, MFM, microstructure, phase separation, chalcogenide

(Some figures may appear in colour only in the online journal)



Original content from this work may be used under the terms of the [Creative Commons Attribution 3.0 licence](#). Any further distribution of this work must maintain attribution to the author(s) and the title of the work, journal citation and DOI.

1. Introduction

Since the discovery of iron-based superconductors in 2008 [1], a rich family of pnictide and chalcogenide compounds

have been found to superconduct [2]. These materials have related crystal structures consisting of puckered Fe-pnictogen (Pn) or Fe-chalcogen (Ch) layers separated by a variety of different species. The superconducting transition temperature (T_c) is found to be influenced by the local structural arrangement, with early work showing a general tendency for T_c to be optimal when the Pn(Ch)–Fe–Pn(Ch) bond angles are close to that for a regular tetrahedron [3] and for T_c to increase with increasing Pn(Ch) height above the Fe plane [4], although later studies have shown that the situation is actually more subtle [2].

The binary FeSe chalcogenide compound, with a superconducting transition temperature (T_c) of ~ 8 K, has the simplest crystal structure consisting of edge-sharing FeSe₄ tetrahedra forming layers. Its transition temperature can be increased in several different ways: partial substitution of about 50% of the Se ions with larger chalcogen ions of Te [5], application of pressure (either externally [6] or by inducing biaxial strains in thin films [7]) and incorporation of alkali metal ions [8] or molecular spacers [9] between the FeSe layers. In addition, monolayer FeSe is found to have a very high T_c of at least 65 K [10, 11]. The alkali metal doped iron chalcogenide superconductors, A_xFe_{2–y}Se₂ (where A = K, Rb, Cs, Tl/K, Tl/Rb), have been a topic of great interest in recent years mainly as a result of their unusual magnetic behaviour combined with the ability to grow large, high quality single crystals which has enabled comprehensive exploration of the fundamental properties using a wide variety of diffraction and spectroscopic analysis techniques [12]. The co-existence of antiferromagnetic ordering with large magnetic moments of $3.3 \mu_B$ per Fe and a Néel temperature well above room temperature with apparently ‘bulk’ superconductivity at about 30 K [13–15] sparked particular interest as it suggests a scenario more similar to the strong coupling seen in high temperature cuprate superconductors [16] than the weak coupling usually considered for iron-based superconductors [17]. Moreover, angle-resolved photoemission spectroscopy (ARPES) studies have shown the absence of a hole pocket in the Fermi surface of the alkali metal doped iron chalcogenides [18–20], indicating that the nesting of hole and electron pockets, often considered to be of fundamental importance in iron-based superconductors, is not a prerequisite for superconductivity in these materials.

The average crystal structure of the A_xFe_{2–y}Se₂ compounds is a direct derivative of the tetragonal I4/mmm ThCr₂Si₂ structure type [21] with lattice parameters $a \sim 4$ Å and $c \sim 15$ Å. However, in superconducting single crystals, a variety of different phases have been observed and their crystal and magnetic structures have been studied in detail using diffraction techniques. There is now a general consensus that two main phases prevalent in superconducting crystals are important for understanding magnetic and electronic properties. The majority phase is typically found to have a chemical formula of A_{0.8}Fe_{1.6}Se₂ and is often referred to by the integer ratios of the elements as the ‘245’ phase. At room temperature and below, the iron vacancies in this phase

form an ordered arrangement with a $\sqrt{5} \times \sqrt{5}$ superstructure, with the supercell being tetragonal with I4/m symmetry and propagation vector along the $[\frac{2}{5}, \frac{1}{5}, 1]$ direction in the I4/mmm basis [22]. Increasing temperature or pressure results in a first order phase transition to an iron-vacancy-disordered phase with the I4/mmm symmetry, with transition temperatures of 489 K–578 K and pressures of 8–11 GPa depending on the alkali metal element, as detailed in a recent review by Krzton-Maziopa *et al* [12]. Several magnetic configurations have been proposed for this phase, with a detailed study using single crystal neutron diffraction with polarized neutrons concluding that only a ‘block spin’ structure is consistent with the experimental results [23]. This configuration consists of blocks of four ferromagnetically ordered Fe²⁺ ions with large spins of $3.3 \mu_B$ aligned along the c -axis of the unit cell. Adjacent blocks are antiferromagnetically aligned in a checkerboard arrangement.

The minority phase is often referred to as the A-122 or iron-vacancy-free phase and has a composition close to A_xFe₂Se₂. A $\sqrt{2} \times \sqrt{2}$ superstructure with propagation vector $[\frac{1}{2}, \frac{1}{2}, 0]$ has been observed in this phase and it was originally described by a P_{mma} model. However for the A = Cs compound, Bozak *et al* have deduced from single crystal synchrotron diffraction studies that the symmetry of this phase is not higher than monoclinic and the apparent $\sqrt{2} \times \sqrt{2}$ superstructure is actually an in-plane projection of diffuse Bragg rods propagating along the c direction [23]. There is a general consensus that, whilst the Fe sublattice is fully occupied in this phase, a significant fraction of the alkali metal sites are vacant, with x values measured to be around 0.6 from neutron diffraction refinement [24, 25], but with NMR results estimating x values as low as 0.3 [26]. A combined Laue neutron diffraction and synchrotron x-ray diffraction study on Cs_xFe_{2–y}Se₂ single crystals by Porter *et al* attribute the $\sqrt{2} \times \sqrt{2}$ superstructure to in-plane Cs vacancy ordering, with every other Cs ion removed to produce stripes along the [110] direction [27]. This 50% occupancy of the alkali metal site is consistent with structural refinements. *Ab initio* calculations suggest that there is no correlation of the Cs ordering between adjacent layers, with the different structural arrangements having similar energies and this uncorrelated picture is supported by the body-centred symmetry of the phase [23]. The Fe ions in this phase have an oxidation state slightly lower than +2, indicating the presence of electron doping [28, 29]. X-ray photoemission (XPS) studies on a series of K_xFe_{2–y}Se₂ crystals support this result, with insulating K_{0.8}Fe_{1.6}Se₂ samples having sharper Fe $2p_{3/2}$ peaks consistent with Fe(II) only, whereas phase separated superconducting crystals have a broader peak with an additional shoulder at slightly lower binding energies attributed Fe in the metallic Fe(0) state [30]. For clarity and consistency, in the remainder of this paper the iron vacancy ordered A_{0.8}Fe_{1.6}Se₂ phase will be referred to as the 245 phase and the iron vacancy free A_xFe₂Se₂ phase will be referred to as the 122 phase.

In addition to the diffraction studies, a very diverse range of techniques have been deployed to study the intrinsic phase separation and the properties of the phases in $A_x\text{Fe}_{2-y}\text{Se}_2$ compounds. These include basic electrical transport, magnetisation and specific heat measurements of the superconducting state, local magnetic moment probes of the bulk material such as muon spin rotation (μSR) [31, 32], NMR [26] and Mössbauer spectroscopies [33, 34], surface sensitive probes such as XPS [30], ARPES [35, 36] and Raman spectroscopy [37, 38], as well as spatially resolved probes including scanning tunnelling microscopy (STM) [39], transmission and scanning electron microscopies (TEM/SEM) [33, 40–42], scanning microfocussed x-ray diffraction ($\mu\text{-XRD}$) [43, 44], scanning photoemission spectroscopy (SPEM) [45], photoemission electron microscopy (PEEM) [46] and magnetic force microscopy (MFM) [46]. This large body of work was comprehensively reviewed by Krzton-Maziopa *et al* in 2016 [12] and here we will confine ourselves to a brief summary of the main findings pertinent to this work. Initial experimental results were somewhat contradictory and confusing; μSR experiments on $\text{Cs}_x\text{Fe}_{2-y}\text{Se}_2$ crystals suggested a spatial phase separation scenario with $\sim 90\%$ of the volume being insulating and antiferromagnetic and the remaining $\sim 10\%$ being the paramagnetic 122 phase associated with superconductivity [31], whereas NMR results on $\text{K}_x\text{Fe}_{2-y}\text{Se}_2$ supported the microscopic co-existence of superconductivity and magnetism [47, 48]. However, later careful NMR studies on $\text{Rb}_x\text{Fe}_{2-y}\text{Se}_2$ by Texier *et al* resolved this by showing that the ^{87}Rb spectra have a broad background with fast transverse relaxation time (T_2) from the antiferromagnetic 245 phase in addition to sharp peaks from the metallic phase [26]. Analytic SEM studies at room temperature have clearly shown a characteristic mesoscopic phase separation, with the minority phase having a striking plate-like morphology forming a 3D network along the $\{113\}$ habit planes (in the $I4/mmm$ basis) [42, 49]. These appear as a square grid of linear features, $\leq 1\mu\text{m}$ wide separated by $\sim 5\mu\text{m}$, aligned along the crystallographic $[110]$ directions on surfaces cleaved parallel to the $(a-b)$ planes. The linear features appear discontinuous (stripey) and 3D sectioning using a focussed ion beam (FIB) microscope show that they consist of a series of finer plates also inhabiting $\{113\}$ crystallographic planes [42]. Energy dispersive x-ray (EDX) analysis in the SEM confirmed that the majority phase has the antiferromagnetic 245 composition, with the minority phase being richer in Fe and more deficient in Rb as expected for the 122 phase. Novel high-resolution electron backscatter diffraction (HR-EBSD) studies [41, 42] and scanning $\mu\text{-XRD}$ studies [43] also confirmed that the minority phase is slightly compressed in the $(a-b)$ plane and elongated in the c direction compared to the matrix. TEM and STM techniques which probe the microstructure at a higher spatial resolution than SEM, show the presence of nano-scale phase separation of the 245 and 122 phases, with high quality cross-sectional HR-TEM suggesting that intergrowths of the two phases form in layers perpendicular to the c -axis in $\text{K}_x\text{Fe}_{2-y}\text{Se}_2$ crystals [39, 40]. This nano-scale phase separation is likely to be in addition to the slightly larger $\{113\}$ aligned platelets observed

in the SEM studies on $\text{Rb}_x\text{Fe}_{2-y}\text{Se}_2$. Robust interpretation of property measurements must take into account the complex, hierarchical microstructure of the superconducting crystals.

A combination of temperature dependent diffraction and differential scanning calorimetry (DSC) [24], Mössbauer spectroscopy [33, 34] and SEM studies [42, 50] have revealed the sequence of phase transformations resulting in the evolution of the two phase microstructure. At high temperatures, the crystals are single phase with the $I4/mmm$ structure and disordered iron vacancies. For $\text{Rb}_x\text{Fe}_{2-y}\text{Se}_2$ on cooling, iron vacancy ordering occurs at $\approx 540\text{K}$ accompanied by a first order transition to $I4/m$ symmetry described above. At slightly lower temperatures ($T_N \approx 517\text{K}$) this iron vacancy ordered structure becomes antiferromagnetic, and on continuing to cool, phase separation occurs at around 489K with the emergence of the iron vacancy free 122 phase within the 245 matrix. An extended x-ray absorption fine-structure (EXAFS) study of $\text{K}_x\text{Fe}_{2-y}\text{Se}_2$ at elevated temperatures revealed that the in-plane Fe-Fe bond length is significantly shorter below the phase separation temperature, consistent with the in-plane compression associated with the 122 phase [51]. Moreover, since the Fe-Se bond length does not change significantly in this temperature range, the decrease in Fe-Fe bond length in the minority phase is argued to be accompanied by an increase in the height of the Se ions above the Fe plane. It was also deduced from the near edge spectra that hybridization between the Fe $3d$ and Se $4p$ states is significantly enhanced below the phase separation temperature in the presence of the 122 phase, influencing the electronic properties. Various annealing studies have shown that, whilst the morphology of the minority phase below the phase separation temperature can be tuned, the volume fraction of the minority phase remains at around 10% [52, 53]. However, by annealing $\text{Rb}_x\text{Fe}_{2-y}\text{Se}_2$ crystals just below the phase separation temperature it is possible to slightly improve the superconducting properties, with magnetisation measurements showing an enhancement in T_c and a narrowing of the superconducting transition [52]. The normal state resistivity of the crystals was also found to be considerably decreased by annealing.

Although there is a considerable amount of indirect evidence that superconductivity occurs in the paramagnetic minority phase, until recently only scanning tunnelling spectroscopy of the nano-scale phase separation in $\text{K}_x\text{Fe}_{2-y}\text{Se}_2$ thin films has given direct evidence of superconductivity localised in the 122 phase [39]. However, it is difficult from this very high spatial resolution study to see how the properties relate to the characteristic mesoscopic phase separation observed in these crystals. To probe superconductivity and antiferromagnetism at the relevant length scales, Hazi *et al* have reported a study combining two different magnetic imaging techniques on $\text{Rb}_x\text{Fe}_{2-y}\text{Se}_2$ crystals. Linear dichroism at the Fe $2p$ edge was imaged with linearly polarised synchrotron x-rays using the wide-field PEEM technique, clearly showing that antiferromagnetic ordering is only present in the matrix. Low temperature MFM used Meissner flux exclusion to confirm that superconductivity is only present in the minority phase features [46]. In addition,

SPEM studies on $\text{K}_x\text{Fe}_{2-y}\text{Se}_2$ have shown clear spatial variations in the occupied density of states within ≈ 1 eV of the Fermi energy, indicating electronic phase separation into a conducting and an insulating phase [45]. However, the spatial maps showing the distribution of the valence band intensity do not clearly reveal the characteristic phase separated microstructure expected in these crystals. In addition, shallow core level spectroscopy carried out in the same study does not reveal the variation in K concentration between the two phases that is expected from the results presented above. Our preliminary SPEM results on $\text{Rb}_x\text{Fe}_{2-y}\text{Se}_2$ crystals reveal the characteristic two phase microstructure, with the minority phase features having a higher intensity in the valence band images than the matrix, indicating that the minority phase is more electrically conductive than the matrix [42].

Therefore, there is now a strong consensus that alkali metal doped iron selenide should be considered to be intrinsically phase separated, with the minority phase being a weakly-coupled electron doped superconductor, similar to other Fe-based superconductors. The superconducting state in these compounds is still of considerable interest, exhibiting unusually low and isotropic values of the lower critical field ($\mu_0 H_{c1} \leq 0.3$ mT) and consequently large penetration depths of $\lambda_{\text{eff}}(0) \approx 1.8$ μm compared with other iron-based and cuprate superconductors [54–56]. Pressure dependent studies also show the unusual emergence of a second superconducting phase at high pressures of around 10 GPa with an even higher T_c of 42 K. It is still not completely clear how this phase separated microstructure which appears to be rather disconnected in the room temperature microscopy [42, 46] exhibits so-called ‘bulk’ superconductivity characterised by a zero-resistance state in transport measurements and a magnetic susceptibility of -1 . One possible explanation is that the stripey plate-like features actually form fully interconnected networks in three-dimensional space, producing macroscopic percolating paths through the crystal and enabling full magnetic shielding of the insulating anti-ferromagnetic phase. However, scanning μ -xrd results suggest the presence of a third ‘interface’ phase that forms at temperatures < 30 K and may also become superconducting at low temperatures, enhancing the macroscopic connectivity, but the sampling depth of 11 μm means that the inclined minority phase features will not be clearly resolved [44]. The valence band SPEM images of $\text{Rb}_x\text{Fe}_{2-y}\text{Se}_2$ taken at around 100 K are also suggestive of a more connected conducting phase, although the probe size may just be too large to resolve the stripey features [42]. Here we report detailed state-of-the-art NanoARPES and magnetic/electrostatic force microscopy of superconducting $\text{Rb}_x\text{Fe}_{2-y}\text{Se}_2$ samples, taken from the same crystals that have previously been characterised by a wide range of techniques including SEM and PEEM to throw light on some of the remaining uncertainties about superconductivity in these very complex crystals.

2. Experimental methods

The experiments reported here have all been carried out on fragments of the same $\text{Rb}_x\text{Fe}_{2-y}\text{Se}_2$ crystal grown by the

Bridgman technique detailed in [57] and cooled from 750 K by quenching at a rate of -200 K min^{-1} . The crystal has an onset T_c value of ≈ 29 K [46]. Since the material is highly air sensitive, the samples were stored in evacuated quartz tubes and freshly cleaved and mounted in an inert atmosphere glove box immediately prior to measurements. For the synchrotron experiments, cleaved crystals were fixed to dedicated holders using conducting epoxy and cured on a hot plate in the glove box. A top post was also attached to the sample surface with conducting epoxy before transferring the sample in a sealed container to the beamline. The sample was cleaved under UHV conditions to produce a fresh, clean surface for analysis.

SPEM and NanoARPES use a sub-micron photon beam raster scanned across the surface of the sample. The emitted photoelectrons are detected at each pixel. Two different beamlines have been used in this work: the NanoARPES end station on the I05 beamline at Diamond Light Source (DLS) and the Antares beamline at Soleil Synchrotron. In both cases a hemispherical Scienta analyser (R4000 at Soleil, DA30 at DLS) has been used, enabling angle-resolved photoemission spectra to be collected. At DLS, zone plate optics at a photon energy of $h\nu = 90$ eV have been used to focus light into a spot 0.7 μm in size, as measured with a knife edge profile width (10%–90%). An overall ARPES energy resolution of ≈ 50 meV is achieved using analyser pass energy of 20 eV, analyser slit of 0.3 mm and monochromator slit of 0.2 mm. At Soleil, $h\nu = 100$ eV was used for the valence band and shallow core level spectroscopy. Zone plate optics gave a nominal lateral resolution of around 120 nm and a pass energy of 20 eV, analyser slit of 0.5 mm and monochromator exit slit of 20 μm were used to obtain a nominal photon beam resolution of 6 meV [58]. A larger pass energy of 100–200 eV was used for core level SPEM, achieving energy resolution of about 200 meV. XPS spectra were fitted with symmetrical 70% Gaussian and 30% Lorentzian peaks using CasaXPS software. The peak positions and FWHM values were kept free in the fit, but the branching ratios of the Se 3d and Rb 4p peaks were fixed at the statistical values of 2/3 and 1/2, respectively.

MFM was performed in an AttoDRY1000 cryostat equipped with a 9 T/3 T superconducting vector magnet using an Attocube MFM-1 microscope with a Point Probe Plus Magnetic Force Microscopy Reflex (PPP1MFMR) tip. The transfer time during which the surface was exposed to air was estimated to be less than 1 min. The sample space was evacuated to a base pressure of 10^{-4} mbar, and backfilled with 30 mbar of He gas. Constant height images were obtained using a lift distance of 30 nm using the procedure detailed in [46]. Electrostatic force microscopy was performed by applying a bias voltage of +2 V to the conducting tip. In these measurements, a negative phase shift (dark contrast) indicates an increase in the attractive force between the sample and the tip (see the supplementary material available online at stacks.iop.org/SUST/32/044005/mmedia).

Vibrating sample magnetometry was performed in a Quantum Design PPMS equipped with a 16 T superconducting magnet. Energy dispersive x-ray (EDX) analysis was carried out in a Zeiss Merlin FEGSEM equipped with a

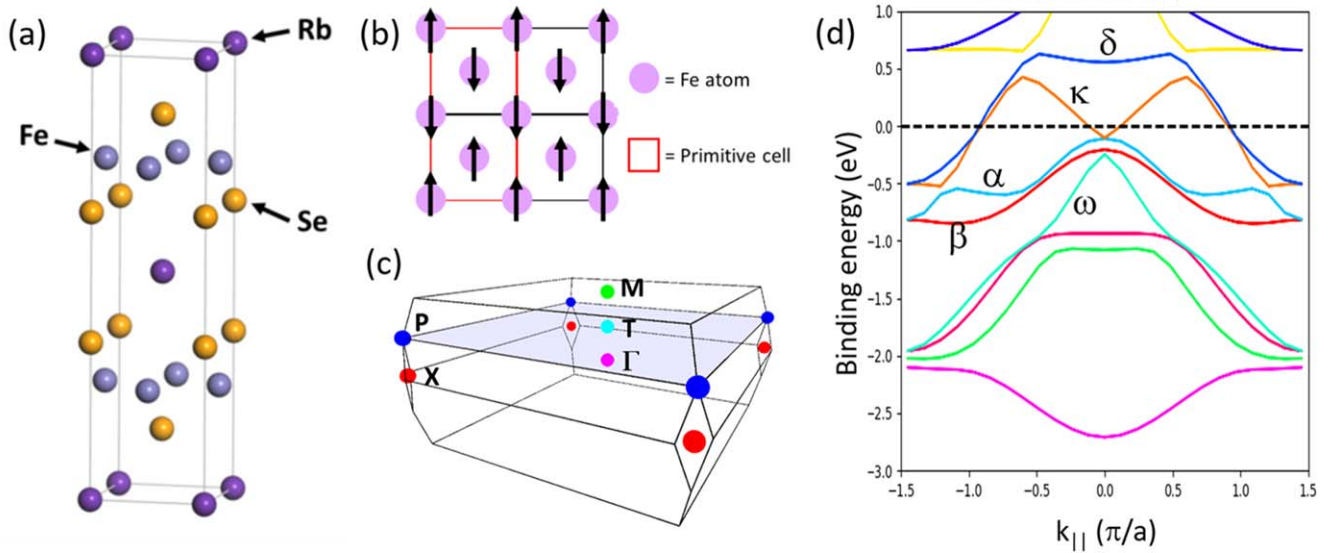


Figure 1. (a) Crystal structure of Rb-122. (b) Bi-collinear arrangement of Fe magnetic moments. (c) Schematic diagram of the body-centred tetragonal Brillouin zone applicable for RbFe_2Se_2 crystal with the high symmetry points labelled. (d) P-T-P Brillouin zone cut calculated using DFT with the Fe 3d bands labelled.

150 mm² Oxford Instruments x-max detector at 10 kV and analysed using Oxford Instruments Aztec software.

Density functional theory (DFT) calculations were performed with the CASTEP software [59] (version 17.1) and employed the Perdew–Burke–Ernzerhof functional [60], Ultrasoft pseudopotentials [61] and a planewave basis-set with a maximum energy of 800 eV. Density of states were calculated using the OptaDOS software [62]. Modelling of various arrangements of the Fe magnetic moment in the 122 structure (figure 1(a)) determined that the antiferromagnetic bi-collinear structure shown in figure 1(b) has the lowest enthalpy, in agreement with Yan *et al* [63].

3. Valence band spectromicroscopy

The valence band of $\text{Rb}_x\text{Fe}_{2-y}\text{Se}_2$ is complex, with contributions from the five Fe 3d electron bands shown in figure 1(d). The NanoARPES end station at DLS has been used to investigate experimentally the valence band (VB) dispersion of the two separate phases in $\text{Rb}_x\text{Fe}_{2-y}\text{Se}_2$ crystals at 30 K. Figure 2(a) shows the Fermi surface map taken using the macrofocussing mirror which has a large spot size and therefore gives an aggregate signal from both phases. The electron pockets at the T and P points in the Brillouin zone (BZ) are clearly visible, consistent with the previous results of Maletz *et al* [36]. Using the Fermi surface map, the crystal was aligned to measure the dispersion along the P-T-P direction, shown in figure 2(b). The band structure calculated using DFT for the RbFe_2Se_2 phase is in good agreement with the data when a renormalisation factor of 3 is used. The strongest feature within 0.2 eV of the Fermi surface is around the T point, originating from a combination of the κ , α , β and ω bands, labelled in figure 1(d). Liu *et al* found that the κ weak electron-like band is derived from the Fe $3d_{xy}$ orbitals admixed with Se $4p_z$ orbitals, whilst the hole-like α and β

bands are mainly derived from the Fe $3d_{xz}$ and $3d_{yz}$ orbitals and are also seen in (Ba,K)-122 pnictide and Fe(Se,Te) chalcogenide superconductors [64]. The ω band is derived from Fe $3d_{3z^2-r^2}$ and is more strongly dispersive than the α and β bands. The feature around the P point has components from the electron-like κ band previously discussed and the δ band which has complex orbital character.

VB SPEM images have been measured using zone plate optics to reduce the spot size of the incident light to ≈ 700 nm. The map in figure 3(a) shows the intensity of photoelectrons originating from states within a narrow binding energy range close to the Fermi energy (-0.5 – 0 eV), integrated over the detector angular range of $\pm 15^\circ$ (i.e. over all $k_{||}$ values along the P-T-P direction in the BZ). A square array of bright features is clearly visible. This corresponds to the characteristic network of superconducting minority phase shown in figure 3(b) and discussed in detail elsewhere [42, 46]. The intensity of the photoelectrons has been used to threshold the brightest and darkest 20% of the VB map, highlighting the superconducting phase (blue) and the matrix (red) respectively in figure 4(a). The reconstructed P-T-P BZ cuts from the blue regions shown in figure 4(b) is very similar to the data obtained using the macro-mirror with a much larger spot size in figure 2(b). In contrast, there is almost no contribution to the VB from the red regions of the map (figure 4(c)). This is the first time that such clear VB dispersions have been shown from the separate phases in $\text{Rb}_x\text{Fe}_{2-y}\text{Se}_2$ crystals, confirming that the VB features observed using larger spot sizes originate from the minority phase alone.

It is interesting to note that the features visible in the VB map in figure 3, taken at 30 K, do not have the stripy appearance seen in the SEM micrographs or PEEM images taken at room temperature [46]. There are two possible reasons for this: either the spatial resolution of the NanoARPES is not good enough to resolve the stripeyness of the features, or there is an influence of temperature on the electronic properties of sample, with the narrow regions between the fine-scale stripes becoming

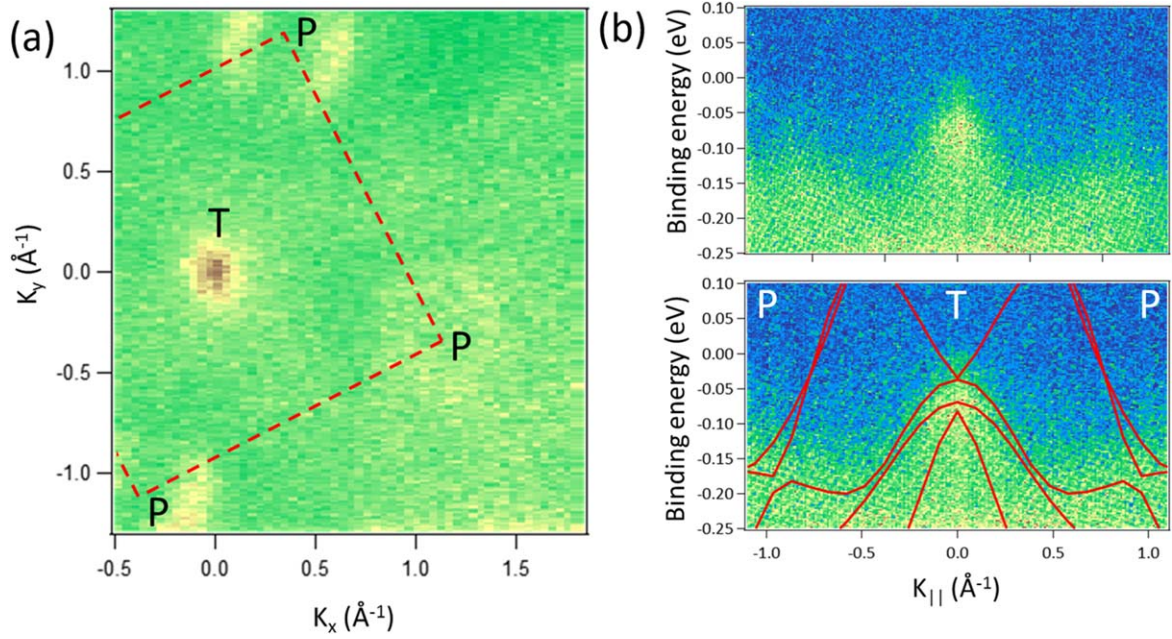


Figure 2. ARPES data taken using the macromirror on the DLS NanoARPES beamline at $h\nu = 90$ eV. (a) Fermi surface map generated from an energy range of 0.2 eV around the Fermi energy. (b) P–T–P Brillouin zone cut taken in fixed mode with the calculated bands renormalised by a factor of 3 superimposed in the lower panel.

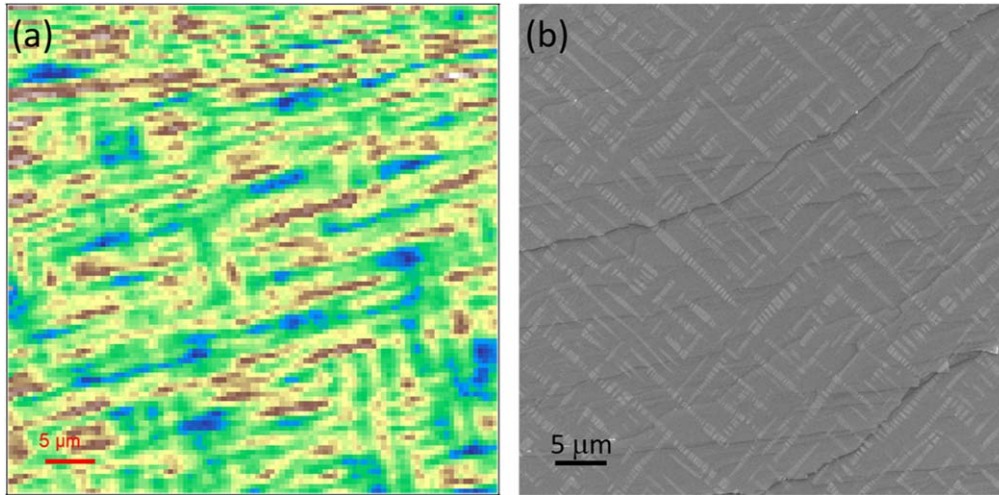


Figure 3. (a) VB spatial map taken at the DLS NanoARPES end station with $h\nu = 90$ eV. (b) Secondary electron image of a similar crystal taken using a JEOL 6500F SEM.

conducting/superconducting at low temperature, as suggested by Ricci *et al* [44]. VB SPEM images taken at Soleil Synchrotron comparing the morphology of the conducting phase at low temperature and room temperature are shown in figure 5. Whilst it is possible that the features in the room temperature image have a slightly more discontinuous appearance, the comparison of these images does not provide conclusive evidence for the second scenario.

4. Magnetic force microscopy

To investigate the morphology of the superconducting phase more closely, MFM has been carried out at a temperature of

around 4.6 K, well below T_c . Figure 6 shows a series of constant height images taken with a lift distance of 30 nm from the same area of the sample. The sample was initially zero field cooled from above T_c to point A on the magnetisation curve shown in figure 7. The contrast in this phase image is purely topographical, with dark contrast arising from raised features. On applying a field of 100 mT in the positive sense (point B), the characteristic microstructure clearly emerges, with the minority phase appearing bright. This corresponds to the presence of a repulsive force between the tip and surface in these regions, confirming that they are superconducting in nature. Note that the images are shown on different contrast scales; the slight topographical contrast (e.g. dark circular features) can still be made out in image B but the magnetic contrast from the superconducting

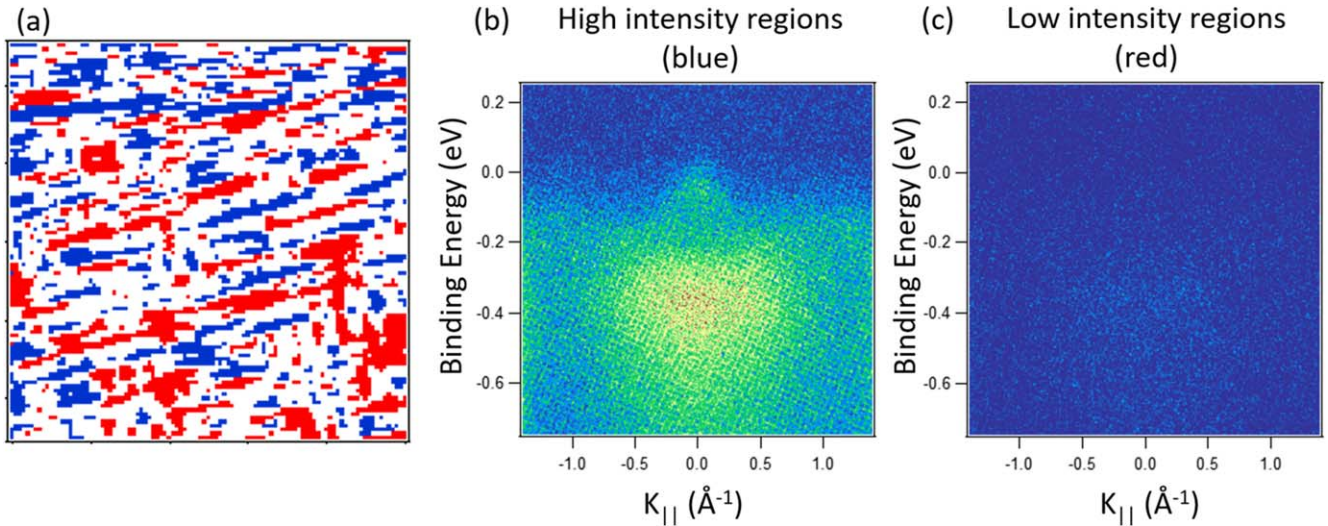


Figure 4. (a) Map showing highest intensity (blue) and lowest intensity (red) regions of the VB map, identifying the 122 superconducting phase and the matrix region respectively. P–T–P BZ cuts generated from the (b) high intensity and (c) low intensity regions using the same colour scale.

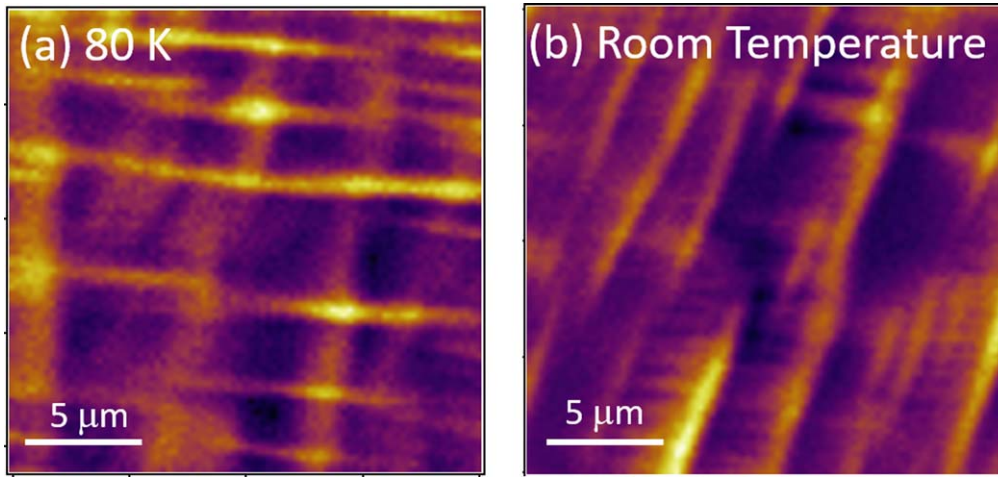


Figure 5. VB spatial maps taken at the Antares beamline, Soleil Synchrotron at (a) 80 K and (b) room temperature.

phase dominates. Increasing the applied field further to point C, the contrast has increased slightly as a result of the larger applied field. Sweeping the field down to -50 mT, image C shows the magnetic contrast is reversed, with the superconducting features now appearing dark. This is because the applied field is now in the opposite direction to the magnetisation of the tip. Increasing the applied field in the negative sense (to -100 mT) reverses the magnetisation direction of the tip as the coercive field of the Co-alloy coating is surpassed [65]. Therefore, in image E the superconducting features appear bright once more. Sweeping back to 0 mT the features become less distinct, and reappear on application of a field in the positive sense, with the contrast reversing again as the magnetisation direction of the tip flips back (image I). This interpretation was confirmed by imaging above T_c at 35 K (see supplementary material).

As can clearly be seen in images B, C, E and I, the bright minority phase features appear discontinuous, as in the room temperature microscopy. It is also worth noting that a dark shadow can be observed to one side of each of the

superconducting plates. This is attributed to the fact that the superconducting plates lie on the $\{113\}$ planes of the crystal, at an angle to the $(a-b)$ plane. The magnetic field is therefore concentrated near the surface on one side of the superconducting features, as shown schematically in figure 8. The electrostatic interaction between the tip and the sample was also investigated in zero field by applying a tip bias of $+2$ V. In these images the conducting features are expected to appear dark, as electrons are free to migrate to the top surface in response to the electric field of the tip resulting in an attractive electrostatic force. As shown in figure 9, the features appear dark confirming that the crystals consist of a conducting minority phase within an insulating matrix.

5. Core level spectromicroscopy

In addition to probing the valence band, synchrotron-based SPEM allows shallow core level spectra from the same regions

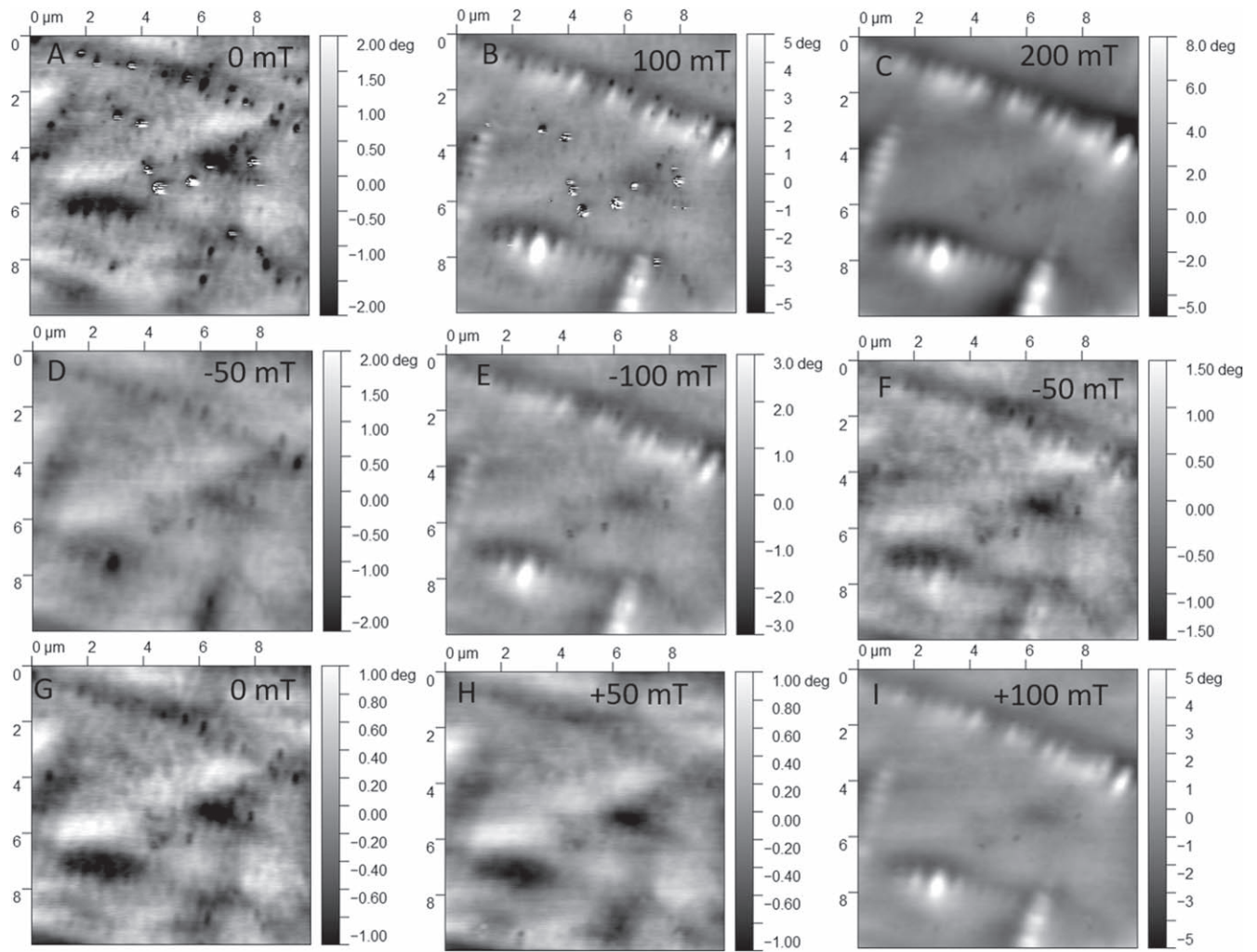


Figure 6. Constant height MFM images taken with a lift height of 30 nm. Sample was zero field cooled to 4.6 K and images were taken as the applied field was changed.

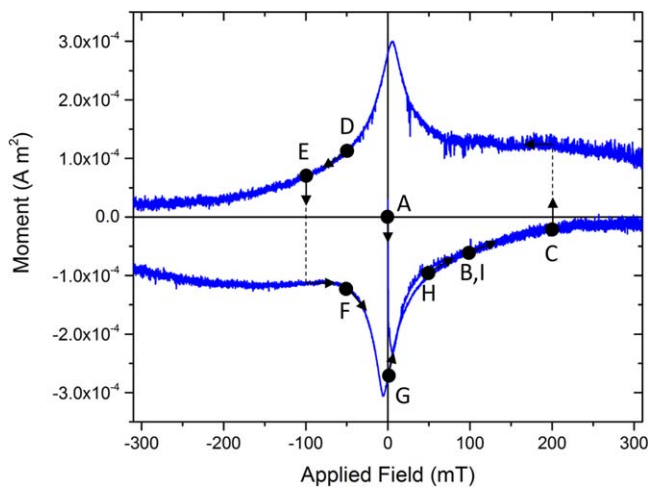


Figure 7. Magnetisation loop from $\text{Rb}_x\text{Fe}_{2-y}\text{Se}_2$ crystal at 4.2 K with the paramagnetic background removed.

of the sample to be mapped. First the overlapping Fe 3*p* and Se 3*d* peaks are considered in detail. The data in figure 10 have been obtained from the same $20 \times 20 \mu\text{m}$ area as the VB map in figure 5(a). The spectra reconstructed from the minority and

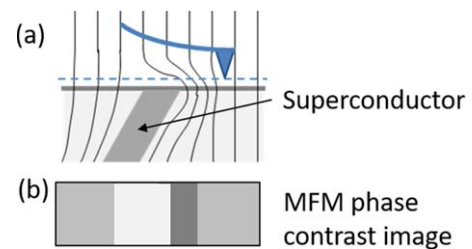


Figure 8. Schematic diagrams of (a) the magnetic field distribution around inclined superconducting feature with the position of the MFM tip during constant height measurement indicated by the blue dotted line, and (b) the resulting MFM phase contrast image, showing the dark region to one side of the bright superconducting feature where the expelled field is concentrated.

matrix phase regions clearly show the presence of two discernible peaks at slightly different binding energies. Spatial maps generated from different energy windows are striking, not only revealing the classic microstructure of the crystal but also showing reverse contrast between the middle and high binding energy regions; in the middle energy range the features appear bright, whereas in the high binding energy range the features appear dark. Good fits have been obtained to the spectra by

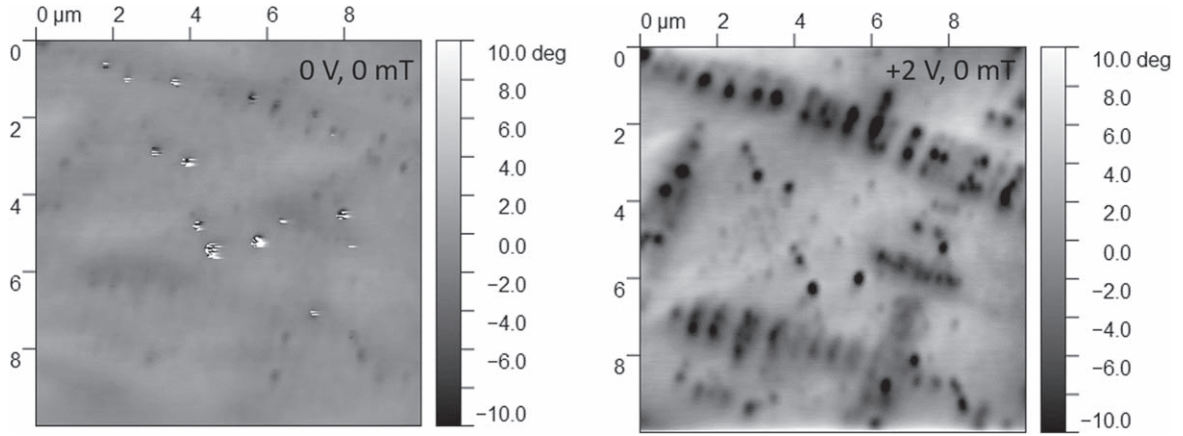


Figure 9. Constant height AFM images at 4.6 K in zero applied field with (a) no tip bias, (b) +2 V tip bias.

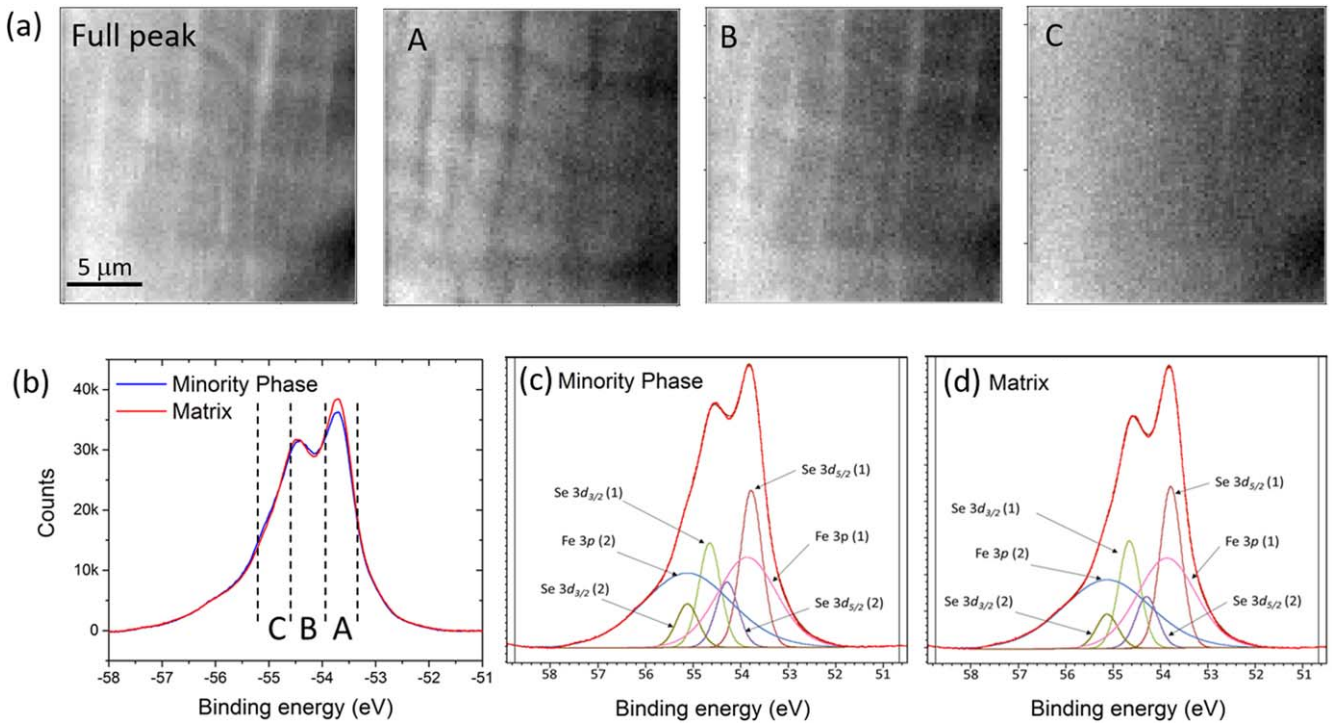


Figure 10. (a) Core level spatial maps generated using different energy windows. (b) Fe 3p and Se 3d sum spectrum from the entire map with the energy windows indicated. (c) and (d) show the fits for the spectra reconstructed from the minority and matrix phases, respectively.

including two symmetric Fe 3p peaks and two pairs of Se $3d_{5/2}/3d_{3/2}$ doublets. The spin-orbit splitting of ≈ 0.85 eV of the Se 3d in our fits is consistent with the literature value of 0.86 eV [66], and the branching ratio has been fixed at $\frac{2}{3}$ as this is the statistical value expected from the relative degeneracy of the states. Tables 1 and 2 give the results of the peak fitting for spectra reconstructed from the minority phase and the matrix. The main difference between the two spectra is the relative intensities of the two Se doublets; the minority phase has a lower fraction of the lower binding energy doublet than the matrix. This is consistent with the findings of Liu *et al* in their study of K-doped FeSe thin films in which the shift of Se 3d to lower binding energy in the $245 \text{ K}_x\text{Fe}_{2-y}\text{Se}_2$ phase has been attributed to the bonding being more three-dimensional in character compared to the 2D bonding in FeSe [67].

The Fe 3p contribution to the peak has been fitted using two symmetric peaks, allowing the peak positions and areas to vary freely in the fits. It is noted that there is a slight change in the relative peak areas in the spectra from the two phases, with a slightly higher proportion of the high binding energy peak in the minority phase than in the matrix. Robust physical interpretation of this is difficult because both the precise chemical environment of the Fe atoms/ions and their oxidation state will result in the overlapping peaks observed here [68]. However, the Fe 2p spectra taken from the same sample using a larger spot size have been reported previously [46], and are similar to spectra from metallic Fe. Therefore, the higher binding energy contribution is more likely to result from a different chemical environment than from the presence of Fe ions in the 3+ oxidation state. Interestingly, the ratio of

Table 1. Binding energy (BE), peak area and full-width half-maximum (FWHM) peak fitting results of the Se 3d/Fe 3p peak.

		Minority phase			Matrix		
Peak		BE (eV)	Area	FWHM (eV)	BE (eV)	Area	FWHM (eV)
Se 3d	$j = \frac{5}{2}$ (1)	53.78	11 841	0.54	53.78	12 792	0.53
	$j = \frac{3}{2}$ (1)	54.65	7898	0.54	54.65	8532	0.53
	$j = \frac{5}{2}$ (2)	54.29	5045	0.55	54.29	4186	0.55
	$j = \frac{3}{2}$ (2)	55.12	3365	0.55	55.12	2792	0.55
Fe 3p	(1)	53.86	18 512	1.47	53.86	22 374	1.45
	(2)	55.12	23 014	2.20	55.12	22 374	2.19

Table 2. Summary of the XPS Se 3d/Fe 3p results for the minority phase and the matrix.

	Minority phase	Matrix
Spin-orbit splitting Se 3d (1)	0.87 eV	0.87 eV
(2)	0.83 eV	0.83 eV
Chemical shift Se 3d	0.47–0.51 eV	0.47–0.51 eV
Area ratio Se (1)/Se (2)	2.3	3.1
Area ratio Fe (1)/Fe (2)	0.80	0.87
Area Fe (total)/Se (total)	0.68	0.68

the total areas of the Fe 3p and the Se 3d peaks show very similar values in the spectra from both regions of the sample, suggesting there is no significant difference in the relative concentration of Fe and Se in the minority and matrix phases.

Spatial maps of the Rb 4p peak have also been measured from the same area of the sample. As can be seen in figure 11(a) the characteristic features of the microstructure are not clearly visible in the Rb 4p map. In order to compare subtle differences in the Rb 4p spectra, the VB map from the same area was used to generate two masks shown in figure 11(d); the mask for minority phase was generated using 20% by area of the most intense pixels, and mask for majority matrix phase includes 20% by area of the least intense pixels. These masks were applied to the Rb 4p map to reconstruct spectra from the two phases. The very small difference between the matrix and minority phase spectra is statistically negligible after background subtraction (see supplementary material).

6. Discussion

The detailed MFM study has clearly shown that the superconducting phase has a stripy morphology consistent with the room temperature electron microscopy of crystals (from the same batch) [42]. The SPEM studies using the NanoARPES instruments on the I05 beamline at DLS and on the Antares beamline at Soleil Synchrotron do not clearly resolve the stripy morphology of the superconducting phase. This is probably because the lateral spatial resolution of these instruments is not good enough to resolve these fine-scale features. However, photoemission spectroscopy is a very surface sensitive technique; electrons with kinetic energies

between 20 and 200 eV have inelastic mean free path values in solids of about 5 Å [69, 70], resulting in sampling depths as small as one to two atomic monolayers between solid state and vacuum. Therefore it is possible that the cleaved surface is not representative of the bulk crystal. The core level SPEM images also suggest that there is not a dramatic difference in the Fe:Se ratio or the Rb content in the two different phases. This was also observed in an earlier SPEM study by Bendele *et al* on related $K_x\text{Fe}_{2-y}\text{Se}_2$ crystals in which Se 3d and K 3p maps were found to be featureless [45]. For comparison purposes SEM/EDX analysis on the same as-grown crystals is shown in figure 12. The minority phase has a slightly higher Fe content and lower Rb content than the matrix, although the difference in chemical composition is not as dramatic as reported previously for annealed crystals in which the minority phase features are significantly larger making quantitative analysis more reliable [42]. The Se content is uniform throughout the crystal. Monte Carlo modelling using Casino v2.5.1.0 software reveals 90% of the emitted x-rays originate from a region of radius ≈ 40 nm and depth ≈ 400 nm for the 10 keV electron beam used in this experiment (see supplementary material). Therefore, EDX gives information about the bulk composition with good lateral resolution, whereas XPS gives information of the surface chemistry with poorer lateral resolution. We can speculate that the chemistry of the cleaved surface of the crystal may be different to the bulk. For instance, the intercalated Rb is very mobile and is known to readily diffuse to the surface if there is an availability of oxygen in the environment. In addition, in both this NanoARPES study at DLS and in our previous PEEM experiment [46] the surface was observed to degrade even in ultra high vacuum over extended time periods, which supports the argument that the surfaces are not stable.

The influence of sub-stoichiometric Rb occupation in the 122 structure has been explored by performing DFT calculations on supercells with different vacancy fractions and ordering. For 50% Rb occupation, in the lowest enthalpy ordered structure the Rb atoms occupy (110) planes, as shown in figure 13(a). This is consistent with the results of Porter *et al* on the Cs-122 system [27]. The total density of states (DOS) derived from the calculations of the lowest enthalpy structures shows that there are only subtle differences between the 25%, 50% and 75% Rb occupation structures, but the 100% Rb (vacancy-free) structure has a significantly smoother density of states profile, as shown in figure 13. Introduction of vacancies can also be seen to increase

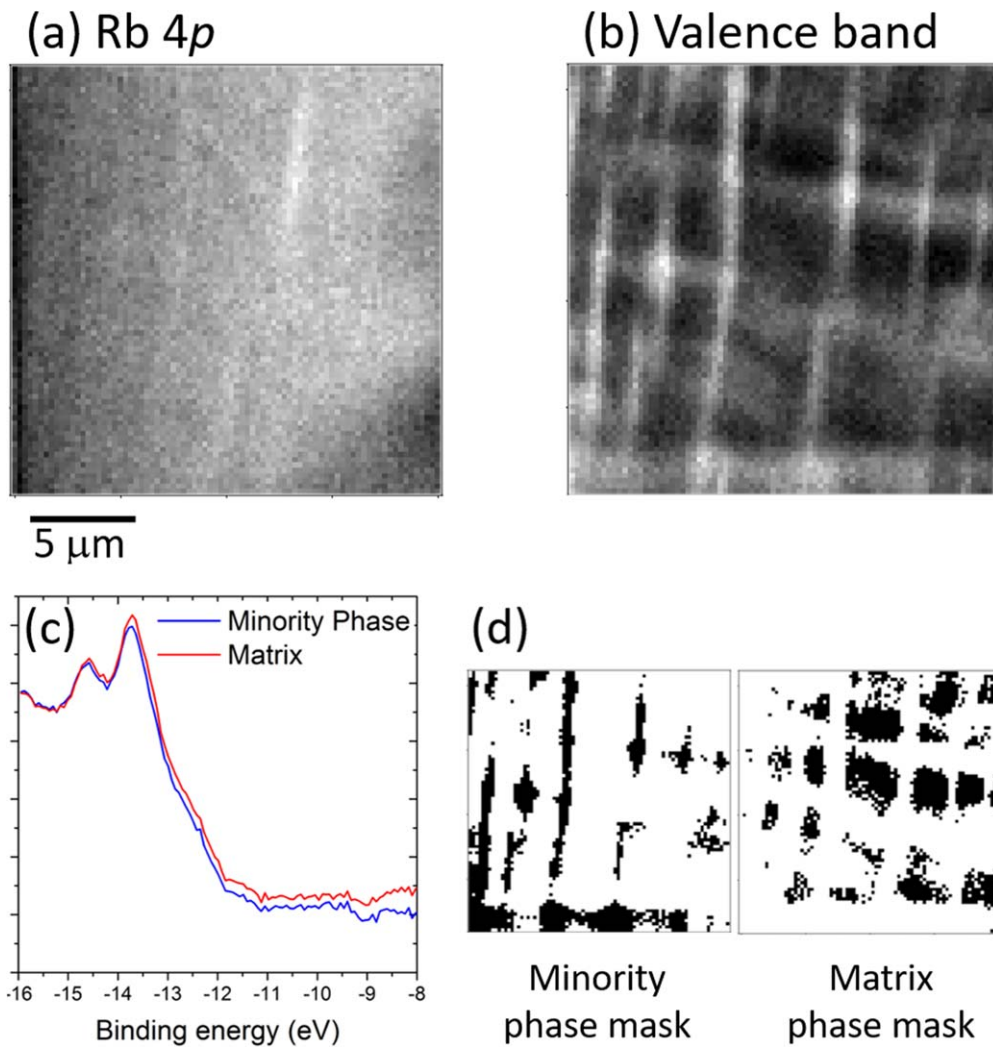


Figure 11. (a) Rb 4p spatial map. (b) VB map from the same area of the sample. (c) Rb 4p spectra reconstructed using masks (d) generated from the VB map.

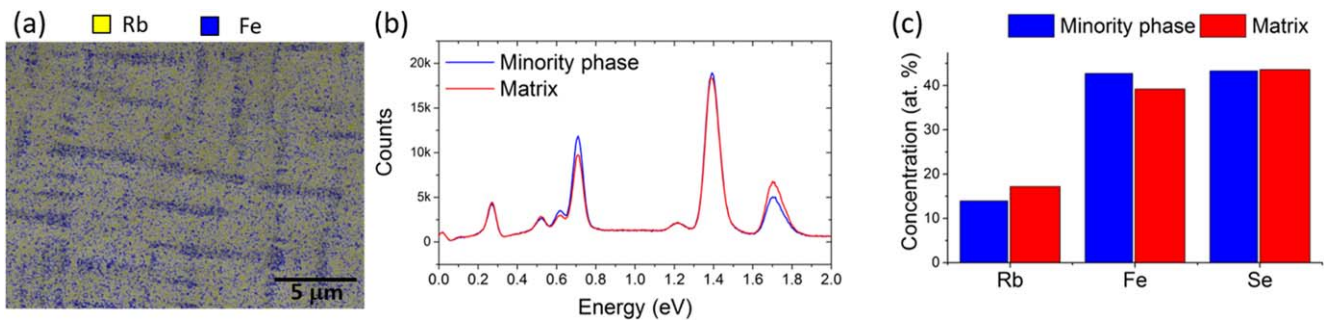


Figure 12. (a) EDX elemental maps taken at 10 kV. (b) EDX spectra reconstructed from minority phase and matrix regions of the sample. (c) Chemical compositions measured by EDX for each phase.

the DOS in the low binding energy range (within 0.2 eV of the Fermi level). The experimental energy dispersive curve has been reconstructed from the minority phase region of the VB map shown in figure 11(b) by averaging over the entire angular range of the detector. However, owing to the broad nature of the experimental data, it is not possible to make a definitive statement about which structural model is more representative.

7. Conclusions

This study has used a combination of synchrotron SPEM and MFM to explore the electronic structure, magnetic properties and chemistry of the separate co-existing phases in $\text{Rb}_x\text{Fe}_{2-y}\text{Se}_2$ single crystals. Consistent with previous studies, the minority phase is clearly shown to have a higher occupied

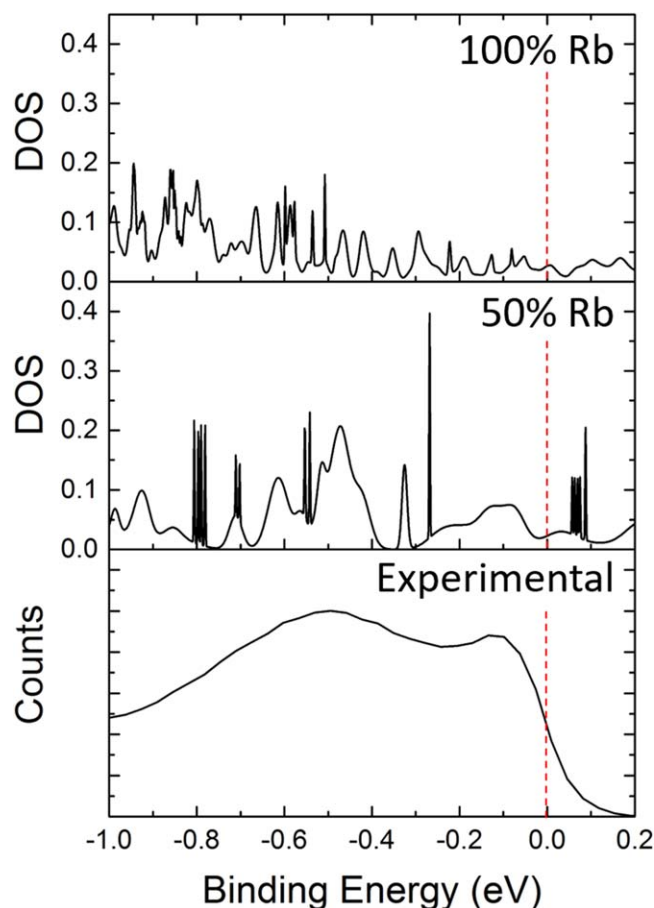


Figure 13. Calculated density of states for the 100% Rb and 50% Rb vacancy structures compared with the experimental energy dispersive cut derived from the superconducting phase regions of the Soleil NanoARPES data.

density of states at the Fermi level, with good agreement between the experimental band dispersion and the DFT calculations. However, the microstructure appears to be a network of continuous features from the VB maps. The MFM study confirms the minority phase is superconducting in nature and has a stripey, discontinuous morphology similar to that observed in previous room temperature microscopy studies. The difference in the morphology of the superconducting phase has been attributed to the lower lateral spatial resolution of the NanoARPES compared to MFM and electron microscopy. Since the crystals are found to have bulk superconducting properties in magnetisation measurements and exhibit zero resistance in transport measurements, the minority superconducting phase must be sufficiently interconnected in three-dimensions to allow macroscopic supercurrent transport even though the 2D picture from the cleaved surface suggest the features are discontinuous. The nature of the interphase region between the superconducting platelets is still a question of debate, as higher resolution spectroscopic techniques are required to study this effectively and the extreme air sensitivity of the samples makes reliable TEM very difficult.

Core level spectromicroscopy reveals that there is no dramatic difference between the chemical composition of the

two phases, at least in the surface region probed by this technique. There are subtle differences in the Se 3d spectra, with the minority phase having a larger contribution from the high binding energy state which has been associated with the dominance of two-dimensional bonding within FeSe layers [67]. In contrast, the matrix has a larger contribution from the low binding energy state associated with the three-dimensional bonding in the 245 Fe vacancy ordered phase. The minority phase is also found to have a slightly higher Rb 4p intensity than the matrix, which is consistent with previous neutron studies which find an $x \approx 0.6$ in $\text{Rb}_x\text{Fe}_{2-y}\text{Se}_2$ [24].

More generally, this study has demonstrated that the combination of nano-focussed ARPES and MFM are powerful techniques for understanding the electronic and magnetic properties of inhomogeneous superconductors, with the characteristic morphology of the phase separation in $\text{A}_x\text{Fe}_{2-y}\text{Se}_2$ making this a particularly good material for making direct comparisons between different imaging techniques. Since phase separation and spatial inhomogeneity is a common theme in the iron-based superconductors, these techniques will be valuable in the study of other novel superconductors.

Acknowledgments

We acknowledge support from the UKCP consortium funded by EPSRC (EP/K013564/1). We are grateful to the UK Materials and Molecular Modelling Hub for computational resources, which is partially funded by EPSRC (EP/P020194/1). SS is grateful for support from the Oxfordshire Local Enterprise Partnership as part of the Oxford Centre for Applied Superconductivity. We thank Diamond Light Source for access to beamline I05 (NT19816) and MC Asensio and J Avila at the Antares beamline Soleil Synchrotron (20141199) that contributed to the results presented here. Data in support of this paper is available at the Oxford Research Archive (<https://ora.ox.ac.uk/>).

ORCID iDs

P Dudin <https://orcid.org/0000-0002-5971-0395>

A Krzton-Maziopa <https://orcid.org/0000-0002-0223-0614>

S C Speller <https://orcid.org/0000-0002-6497-5996>

References

- [1] Kamihara Y, Watanabe T, Hirano M and Hosono H 2008 Iron-based layered superconductor $\text{La}[\text{O}_{1-x}\text{F}_x]\text{FeAs}$ ($x = 0.05-0.12$) with $T_c = 26$ K *J. Am. Chem. Soc.* **130** 3296
- [2] Hosono H and Kuroki K 2015 Iron-based superconductors: current status of materials and pairing mechanism *Physica C* **514** 399
- [3] Lee C-H, Iyo A, Eisaki H, Kito H, Fernandez-Diaz M T, Ito T, Kihou K, Matsuhata H, Braden M and Yamada K 2008 Effect of structural parameters on superconductivity in

- fluorine-free LnFeAsO_{1-y} ($\text{Ln} = \text{La}, \text{Nd}$) *J. Phys. Soc. Japan* **77** 083704
- [4] Kuroki K, Usai H, Onari S, Arita R and Aoki H 2009 Pnictogen height as a possible switch between high- T_c and low- T_c nodal pairings in the iron-based superconductors *Phys. Rev. B* **79** 224511
 - [5] Yeh K W *et al* 2008 Tellurium substitution effect on superconductivity of the α -phase iron selenide *Europhys. Lett.* **84** 37002
 - [6] Mizuguchi Y, Tomioka F, Tsuda S, Yamaguchi T and Takano Y 2008 Superconductivity at 27 K in tetragonal FeSe under high pressure *Appl. Phys. Lett.* **93** 152505
 - [7] Bellingeri E, Pallecchi I, Buzio R, Gerbi A, Marre D, Cimberle M R, Tropeano M, Putti M, Palenzona A and Ferdeghini C 2010 $T_c = 21$ K in epitaxial $\text{FeSe}_{0.5}\text{Te}_{0.5}$ thin films with biaxial compressive strain *Appl. Phys. Lett.* **96** 102512
 - [8] Guo J G, Jin S F, Wang G, Wang S C, Zhu K X, Zhou T T, He M and Chen X L 2010 Superconductivity in the iron selenide $\text{K}_x(\text{Fe}_2\text{Se})_2$ ($0 \leq x \leq 1.0$) *Phys. Rev. B* **82** 180520(R)
 - [9] Ying T P, Chen X L, Wang G, Jin S F, Zhou T T, Lai X F, Zhang H and Wang W Y 2012 Observation of superconductivity at $30 \sim 46$ K in $\text{A}_x\text{Fe}_2\text{Se}_2$ ($\text{A} = \text{Li}, \text{Na}, \text{Ba}, \text{Sr}, \text{Ca}, \text{Yb}, \text{and Eu}$) *Sci. Rep.* **2** 426
 - [10] He S *et al* 2013 Phase diagram and electronic indication of high-temperature superconductivity at 65 K in single-layer FeSe films *Nat. Mater.* **12** 605
 - [11] Ge J-F, Liu Z-L, Liu C, Gao C-L, Qian D, Xue Q-K, Liu Y and Jia J-F 2015 Superconductivity above 100 K in single-layer FeSe films on doped SrTiO_3 *Nat. Mater.* **14** 285
 - [12] Krzton-Maziopa A, Svitlyk V, Pomjakushina E, Puzniak R and Conder K 2016 Superconductivity in alkali metal intercalated iron selenides *J. Phys.: Condens. Matter* **28** 293002
 - [13] Tsurkan V, Deisenhofer J, Gunther A, Krug von Nidder H A, Widmann S and Loidl A 2011 Anisotropic magnetism, superconductivity and the phase diagram of $\text{Rb}_{1-x}\text{Fe}_{2-y}\text{Se}_2$ *Phys. Rev. B* **84** 144520
 - [14] Ying J J *et al* 2011 Superconductivity and magnetic properties of single crystals of $\text{K}_{0.75}\text{Fe}_{1.66}\text{Se}_2$ and $\text{Cs}_{0.81}\text{Fe}_{1.61}\text{Se}_2$ *Phys. Rev. B* **83** 212502
 - [15] Zeng B, Shen B, Chen G F, He B, Wang D M, Li C H and Wen H H 2011 Nodeless superconductivity of single-crystalline $\text{K}_x\text{Fe}_{2-y}\text{Se}_2$ revealed by the low-temperature specific heat *Phys. Rev. B* **83** 144511
 - [16] Yu R, Zhu J-X and Si Q 2011 Mott transition in modulated lattices and parent insulator of $(\text{K}, \text{Ti})_x\text{Fe}_y\text{Se}_2$ superconductors *Phys. Rev. Lett.* **106** 186401
 - [17] Paglione J and Greene R L 2010 High-temperature superconductivity in iron-based materials *Nat. Phys.* **6** 645
 - [18] Mou D *et al* 2011 Distinct Fermi surface topology and nodeless superconducting gap in a $(\text{Ti}_{0.58}\text{Rb}_{0.42})\text{Fe}_{1.72}\text{Se}_2$ superconductor *Phys. Rev. Lett.* **106** 107001
 - [19] Zhang Y *et al* 2011 Nodeless superconducting gap in $\text{A}_x\text{Fe}_2\text{Se}_2$ ($\text{A} = \text{K}, \text{Cs}$) revealed by angle-resolved photoemission spectroscopy *Nat. Mater.* **10** 273
 - [20] Qian T *et al* 2011 Absence of a holelike Fermi surface for the iron-based $\text{K}_{0.8}\text{Fe}_{1.7}\text{Se}_2$ superconductor revealed by angle-resolved photoemission spectroscopy *Phys. Rev. Lett.* **106** 187001
 - [21] Ban Z and Sikirica M 1965 The crystal structure of ternary silicides ThM_2Si_2 ($\text{M} = \text{Cr}, \text{Mn}, \text{Fe}, \text{Co}, \text{Ni}$ and Cu) *Acta Crystallogr.* **18** 594
 - [22] Pomjakushin V Y, Sheptyakov D V, Pomjakushina E V, Krzton-Maziopa A, Conder K, Chernyshov D, Svitlyk V and Shermadini Z 2011 Iron vacancy superstructure and possible room temperature antiferromagnetic order in superconducting $\text{Cs}_x\text{Fe}_{2-x}\text{Se}_2$ *Phys. Rev. B* **83** 144410
 - [23] Bosak A, Svitlyk V, Krzton-Maziopa A, Pomjakushina E, Conder K, Pomjakushin V, Popov A, de Sanctis D and Chernyshov D 2012 Phase co-existence in $\text{Cs}_{0.8}\text{Fe}_{1.6}\text{Se}_2$ as seen by x-ray mapping of reciprocal space *Phys. Rev. B* **86** 174107
 - [24] Pomjakushin V Y, Krzton-Maziopa A, Pomjakushina E V, Conder K, Chernyshov D, Svitlyk V and Bosak A 2012 Intrinsic crystal phase separation in the antiferromagnetic superconductor $\text{Rb}_y\text{Fe}_{2-x}\text{Se}_2$: a diffraction study *J. Phys.: Condens. Matter* **24** 435701
 - [25] Fang M, Wang H, Dong C and Huang Q 2013 Superconductivity and magnetism in $(\text{Ti}, \text{K}, \text{Rb})\text{Fe}_x\text{Se}_2$ *J. Phys.: Conf. Ser.* **449** 012015
 - [26] Texier Y, Deisenhofer J, Tsurkan V, Loidl A, Inosov D S, Friemel G and Bobroff J 2012 *Phys. Rev. Lett.* **108** 237002
 - [27] Porter D G *et al* 2015 Two-dimensional Cs-vacancy superstructure in iron-based superconductor $\text{Cs}_{0.8}\text{Fe}_{1.6}\text{Se}_2$ *Phys. Rev. B* **91** 144114
 - [28] Basca J, Ganin A Y, Takabayashi Y, Christensen K E, Prassides K, Rosseinsky M J and Claridge J B 2011 Cation vacancy order in the $\text{K}_{0.8+x}\text{Fe}_{1.6-y}\text{Se}_2$ system: five-fold cell expansion accommodates 20% tetrahedral vacancies *Chem. Sci.* **2** 1054
 - [29] Sun H *et al* 2015 Soft chemical control of superconductivity in lithium iron selenide hydroxides $\text{Li}_{1-x}(\text{Fe}_x(\text{OH})\text{Fe}_{1-y}\text{Se})$ *Inorg. Chem.* **54** 1958–64
 - [30] Oiwake M, Ootsuki D, Noji T, Hatakeda T, Koike Y, Horio M, Fujimori A, Saini N L and Mizokawa T 2013 Electronic structure and phase separation of superconducting and nonsuperconducting $\text{K}_x\text{Fe}_{2-y}\text{Se}_2$ revealed by x-ray photomission spectroscopy *Phys. Rev. B* **88** 224517
 - [31] Shermadini Z *et al* 2011 Co-existence of magnetism and superconductivity in the iron-based compound $\text{Cs}_{0.8}(\text{Fe}_{0.98}\text{Se})_2$ *Phys. Rev. Lett.* **106** 117602
 - [32] Shermadini Z, Luetkens H, Khasanov R, Krzton-Maziopa A, Conder K, Pomjakushina E, Klaus H-H and Amato A 2012 Superconducting properties of single-crystalline $\text{A}_x\text{Fe}_{2-y}\text{Se}_2$ *Phys. Rev. B* **85** 100501(R)
 - [33] Ryan D H, Rowan-Weetaluktuk W N, Cadogan J M, Hu R, Straszheim W E, Bud'ko S L and Canfield P C 2011 ^{57}Fe Mossbauer study of magnetic ordering in superconducting $\text{K}_{0.80}\text{Fe}_{1.76}\text{Se}_{2.00}$ single crystals *Phys. Rev. B* **83** 104526
 - [34] Ksenofontov V, Wortmann G, Medvedev S A, Tsurkan V and Deisenhofer J 2011 Phase separation in superconducting $\text{Rb}_{0.8}\text{Fe}_{1.6}\text{Se}_2$ probed by Mossbauer spectroscopy *Phys. Rev. B* **84** 180508(R)
 - [35] Chen F *et al* 2011 Electronic identification of the parental phases and mesoscopic phase separation of $\text{K}_x\text{Fe}_{2-y}\text{Se}_2$ superconductors *Phys. Rev. X* **1** 021020
 - [36] Malet J *et al* 2013 Photoemission and muon spin relaxation spectroscopy of the iron-based $\text{Rb}_{0.77}\text{Fe}_{1.61}\text{Se}_2$ superconductor: crucial role of the cigar-shaped Fermi surface *Phys. Rev. B* **88** 134501
 - [37] Lazarević N, Abeykoon M, Stephens P W, Lei H, Bozin E S, Petrovic C and Popović Z V 2012 Vacancy-induced nanoscale phase separation in $\text{K}_x\text{Fe}_{2-y}\text{Se}_2$ single crystals evidenced by Raman scattering and powder x-ray diffraction *Phys. Rev. B* **86** 054503
 - [38] Zhang A M, Xiao J H, Li Y S, He J B, Wang D M, Chen G F, Normand B and Zhang Q M 2012 Two-magnon Raman scattering in $\text{A}_{0.8}\text{Fe}_{1.6}\text{Se}_2$ systems ($\text{A} = \text{K}, \text{Rb}, \text{Cs}, \text{and Ti}$): competition between superconductivity and antiferromagnetic order *Phys. Rev. B* **85** 214508
 - [39] Li W *et al* 2012 Phase separation and magnetic order in K-doped iron selenide superconductor *Nat. Phys.* **8** 126
 - [40] Wang Z, Song Y J, Shi H L, Wang Z W, Chen Z, Tian H F, Chen G F, Guo J G, Yang H X and Li J Q 2011 Microstructure and ordering of iron vacancies in the

- superconductor system $K_yFe_xSe_2$ as seen via transmission electron microscopy *Phys. Rev. B* **83** 140505(R)
- [41] Speller S C, Britton T B, Hughes G M, Krzton-Maziopa A, Pomjakushina E, Conder K, Boothroyd A T and Grovenor C R M 2012 Microstructural analysis of phase separation in iron chalcogenide superconductor *Supercond. Sci. Technol.* **25** 084023
- [42] Speller S C *et al* 2014 High-resolution characterization of microstructural evolution in $Rb_x(Fe_{2-y}Se)_2$ crystals on annealing *Phys. Rev. B* **90** 024520
- [43] Ricci A *et al* 2011 Intrinsic phase separation in superconducting $K_{0.8}Fe_{1.6}Se_2$ ($T_c = 31.8$ K) single crystals *Supercond. Sci. Technol.* **24** 082002
- [44] Ricci A *et al* 2015 Direct observation of nanoscale interface phase in the superconducting chalcogenide $K_xFe_{2-y}Se_2$ with intrinsic phase separation *Phys. Rev. B* **91** 020503(R)
- [45] Bendele M *et al* 2014 Spectromicroscopy of electronic phase separation in $K_xFe_{2-y}Se_2$ superconductor *Sci. Rep.* **4** 5592
- [46] Hazi J, Mousavi T, Dudin P, van der Laan G, Maccheronzi F, Krzton-Maziopa A, Pomjakushina E, Conder K and Speller S C 2018 Magnetic imaging of antiferromagnetic and superconducting phases in $Rb_x(Fe_{2-y}Se)_2$ crystals *Phys. Rev. B* **97** 054509
- [47] Torchetti D A, Fu M, Christensen D C, Nelson K J, Imai T, Lei H C and Petrovic C 2011 ^{77}Se NMR investigation of the $(K_xFe_{2-y}Se)_2$ high- T_c superconductor ($T_c = 33$ K) *Phys. Rev. B* **83** 104508
- [48] Yu W, Ma L, He B, Wang D M, Xia T-L, Chen G F and Bao W 2011 ^{77}Se NMR study of the pairing symmetry and the spin dynamics in $K_yFe_{2-x}Se_2$ revealed by the low-temperature specific heat *Phys. Rev. Lett.* **106** 197001
- [49] Wang Z, Cai Y, Wang Z W, Ma C, Chen Z, Yang H X, Tian H F and Li J Q 2015 Archimedean solidlike superconducting framework in phase-separated $K_{0.8}Fe_{1.6+x}Se_2$ ($0 \leq x \leq 0.15$) *Phys. Rev. B* **91** 064513
- [50] Liu Y, Zing Q, Straszheim W E, Marshman J, Pedersen P, McLaughlin R and Lograsso T A 2016 Formation mechanism of superconducting phase and its three-dimensional architecture in pseudo-single-crystal $K_xFe_{2-y}Se_2$ *Phys. Rev. B* **93** 064509
- [51] Iadecola A, Joseph B, Bendele M, Aquilanti G, Takeya H, Mizuguchi Y, Takano Y, Mizokawa T and Saini N L 2014 Local structure response of phase separation in iron-vacancy order in $K_xFe_{2-y}Se_2$ superconductor *Phys. Rev. B* **90** 174509
- [52] Weyeneth S *et al* 2012 Superconductivity and magnetism in $Rb_xFe_{2-y}Se_2$: impact of thermal treatment on mesoscopic phase separation *Phys. Rev. B* **86** 134530
- [53] Liu Y, Zing Q, Dennis K W, McCallum R W and Lograsso T A 2012 Evolution of precipitate morphology during heat treatment and its implications for the superconductivity in $K_xFe_{1.6+y}Se_2$ single crystals *Phys. Rev. B* **86** 144507
- [54] Bosma S, Puzniak R, Krzton-Maziopa A, Bendele M, Pomjakushina E, Conder K, Keller H and Weyeneth S 2012 Magnetic-field tuned anisotropy in superconducting $Rb_xFe_{2-y}Se_2$ *Phys. Rev. B* **85** 064509
- [55] Lei H and Petrovic C 2011 Anisotropy in transport and magnetic properties of $K_{0.64}Fe_{1.44}Se_2$ *Phys. Rev. B* **83** 184504
- [56] Tsindlekht M I, Felner I, Zhang M, Wang A F and Chen X H 2011 Superconducting critical fields of single-crystalline $(K_{0.73}Fe_{1.68}Se)_2$ *Phys. Rev. B* **84** 052503
- [57] Krzton-Maziopa A, Pomjakushina E and Conder K 2012 Single crystals of novel alkali metal intercalated iron chalcogenide superconductors *J. Cryst. Growth* **360** 155–7
- [58] Avila J, Rizado I, Lorcy S, Fleurier R, Pichonat E, Vignaud D, Wallart X and Asensio M C 2013 Exploring electronic structure of one-atom thick polycrystalline graphene films: a nano angle resolved photoemission study *Sci. Rep.* **3** 2439
- [59] Clark S J, Segall M D, Pickard C J, Hasnip P J, Probert M I J, Refson K and Payne M C 2005 First principles methods using CASTEP *Z. Kristallogr.—Cryst. Mater.* **220** 567–70
- [60] Perdew J P, Burke K and Ernzerhof M 1996 Generalized gradient approximation made simple *Phys. Rev. Lett.* **77** 28
- [61] Vanderbilt D 1990 Soft self-consistent pseudopotentials in a generalized eigenvalue formalism *Phys. Rev. B* **41** 7892–5
- [62] Morris A J, Nicholls R J, Pickard C J and Yates J R 2014 Optados: a tool for obtaining density of states, core-level and optical spectra from electronic structure codes *Comput. Phys. Commun.* **185** 1477–85
- [63] Yan X-W, Gao M, Lu Z-Y and Xiang T 2011 Electronic and magnetic structures of the ternary iron selenides $AFe_{1.5}Se_2$ ($A = Cs, Rb, K, \text{ or } Tl$) *Phys. Rev. B* **84** 054502
- [64] Liu Z-H 2012 Three dimensionality and orbital characters of Fermi surface in $(Tl,Rb)_3Fe_{2-x}Se_2$ *Phys. Rev. Lett.* **109** 037003
- [65] Jaafar M, Asenjo A and Vazquez M 2008 Calibration of coercive and stray fields of commercial magnetic force microscope probes *IEEE Trans. Nanotechnol.* **7** 245
- [66] Moulder J F, Stickle W F, Sobol P E and Bombard K D 1992 *Handbook of X-ray Photoelectron Spectroscopy* (Waltham, MA: Perkin-Elmer Corporation)
- [67] Liu C, Zhao J C, Wang Z O, Qian H J, Wu R, Wang H H, Zhang N and Ibrahim K 2017 Correspondence between the electronic structure and phase separation in a K doped FeSe system *J. Phys.: Condens. Matter* **29** 395503
- [68] Descostes M, Mercier F, Thomat N, Beaucaire C and Gautier-Soyer M 2000 Use of XPS in the determination of chemical environment and oxidation state of iron and sulfur samples *Appl. Surf. Sci.* **165** 288
- [69] Brundle C R 1974 The application of electron spectroscopy to surface studies *J. Vac. Sci. Technol.* **11** 212
- [70] Seah M P and Dench W A 1979 Quantitative electron spectroscopy of surfaces: a standard database for electron inelastic mean free paths in solids *Surf. Interface Anal.* **1** 2